Topology optimization empowered dual-band second-order photonic topological insulators

Yafeng Chen,[1,*] Yuting Yang,[2,3,†] Shiyu Liu,[2] Zhihao Lan,[4] Shanjun Liang,[5] Jie Zhu,[1,‡] and Zhongqing Su[6,§]

[1] *Institute of Acoustics, School of Physics Science and Engineering, Tongji University, 200092 Shanghai, China*
[2] *School of Materials and Physics, China University of Mining and Technology, Xuzhou 221116, China*
[3] *State Key Laboratory of Millimeter Waves, Southeast University, Nanjing 210096, China*
[4] *Department of Electronic and Electrical Engineering, University College London, London WC1E 7JE, United Kingdom*
[5] *School of Professional Education and Executive Development, The Hong Kong Polytechnic University, Kowloon, Hong Kong SAR, China*
[6] *Department of Mechanical Engineering, The Hong Kong Polytechnic University, Kowloon, Hong Kong SAR, China*

(Received 13 December 2024; revised 9 February 2025; accepted 3 April 2025; published 22 April 2025)

Dual-band second-order photonic topological insulators (SPTIs), characterized by multiple corner states, offer exceptional potential for robust multiband manipulation of electromagnetic waves in lower dimensions. However, previous theoretical implementations of dual-band SPTIs have been constrained by limited flexibility, hindering their adaptability for diverse applications. Additionally, experimental validation of these dual-band SPTIs has been lacking. In this study, we introduce a topology optimization method to design SPTIs with customizable dual-band corner states tailored for specific multiband applications. Dual-band SPTIs with customized corner states for manipulating electromagnetic waves of transverse magnetic and electric modes are created. Furthermore, multiple corner states within dual bandgaps are experimentally confirmed. This work opens new avenues for creating customizable photonic devices with dual-band topological features, enabling versatile multiband applications.

DOI: 10.1103/PhysRevApplied.23.044048

I. INTRODUCTION

Photonic topological insulators (PTIs), characterized by topological interface states that are robust against impurities, have garnered significant attention [1–5]. Inspired by topological insulators in electronic materials, a diverse array of PTIs has been achieved, including those based on the quantum Hall effect [6,7], quantum valley and spin Hall effect [8–17], and Floquet PTIs [18–20], *etc.* These PTIs adhere to conventional bulk-boundary correspondence, meaning a system with d-dimensions supports gapless interface states in $d-1$ dimensions. Thereafter, high-order PTIs, which transcend the conventional bulk-boundary correspondence by hosting multidimensional boundary states, have been developed [21,22]. In two-dimensional (2D) systems, second-order PTIs (SPTIs) feature gapped interface states and in-gap corner states. The design of SPTIs is heavily influenced by crystalline symmetry, which plays a crucial role in determining the physical mechanisms. So far, diverse recipes of SPTIs have been realized in different symmetric lattices, such as C_3-symmetric hexagonal and kagome lattices [23–26], C_{6v}-symmetric honeycomb lattice [27], C_4- and C_{4v}-symmetric square lattices [28–36], etc. As SPTIs feature highly localized corner states with robustness, they hold promise for novel photonic applications, including microwave communications [37], topological laser [38], photonic nanocavity with high-quality factor [39,40], and optical elements for nonlinear frequency conversion [35,41].

Toward multiband robust communication of electromagnetic waves, it is highly desirable to develop multiband topological photonic devices (MTPDs) due to their many important application scenarios. Firstly, as frequency acts as an important degree of freedom in photonic communications, MTPDs facilitate complex photonic communications by processing signals across different frequency bands simultaneously, enabling faster and more efficient processing for different specific tasks. Meanwhile, MTPDs with highly localized topological states can be employed

*Contact author: yachen@tongji.edu.cn
†Contact author: yangyt@cumt.edu.cn
‡Contact author: jiezhu@tongji.edu.cn
§Contact author: zhongqing.su@polyu.edu.hk

to develop robust photonic sensors across multiple frequency bands. Moreover, MTPDs with multiple corner states can be used to generate and control multiwavelength light sources, which are valuable for applications such as multiwavelength interferometry, multimode optical fiber, and nonlinear multiwave mixing. Kim and Om theoretically proposed an SPTI, designed using a physics-inspired method, which hosts multiband gapped topological interface states and in-gap corner states for transverse magnetic (TM) modes [42]. Chen *et al*. developed an inversely designed SPTI with fully connected dielectric materials that supports multiband corner states for transverse electric (TE) modes [34]. Despite these advancements, the bandgaps—and particularly the order of these bandgaps—used to host corner states in these multiband SPTIs cannot be controlled on demand, limiting their flexibility for various practical applications. Meanwhile, the order of the bandgap is highly related to the topology property of the unit cell (UC). It is, therefore, desirable to engineer the UC with a specific and on-demand order to further construct the SPTI. Furthermore, current multiband SPTIs have yet to be experimentally validated. To overcome these challenges, we propose a topology optimization approach—an inverse method proven effective in designing novel photonic structures [43–45]—to create dual-band SPTIs. This approach allows for the on-demand customization of dual bandgaps to support corner states. We demonstrate tightly localized dual-band corner states within different customized dual bandgaps for TM and TE modes and experimentally validate multiple corner states within these dual bandgaps. Our work offers a pathway for customizing multiband topological photonic devices to meet specific application requirements.

II. RESULTS AND DISCUSSION

A. Design methodology

In Sec. 1 within the Supplemental Material [46], we establish a rule under which the photonic crystal with odd-order bandgaps can be used to construct the SPTI. Building on this fact, the topology optimization approach, which is an intelligent method to seek the most efficient material layout to satisfy performance objectives while adhering to constraints and, thus, enables more efficient, creative, and effective solutions, is developed to design photonic crystals (PCs) with customized double odd-order bandgaps. By selecting two UCs from these designed PCs, we can construct SPTIs with corner states within dual bandgaps. The propagation of electromagnetic waves in two-dimensional dielectric PCs can be decoupled with TM and TE modes, governed by [47,48]

$$\mathrm{TM} = (\nabla + i\mathbf{k}) \cdot ((\nabla + i\mathbf{k})E(\mathbf{r})) = \varepsilon(\mathbf{r})\left(\frac{\omega}{c}\right)^2 E(\mathbf{r}), \tag{1a}$$

$$\mathrm{TE} = (\nabla + i\mathbf{k}) \cdot \left(\frac{1}{\varepsilon(\mathbf{r})}(\nabla + i\mathbf{k})H(\mathbf{r})\right) = \left(\frac{\omega}{c}\right)^2 H(\mathbf{r}), \tag{1b}$$

where $\mathbf{r}$ represents the position vector, ω denotes the eigenfrequency, c is the speed of light, $\varepsilon(\mathbf{r})$ refers to the dielectric function, and $\mathbf{k} = (k_x, k_y)$ is the wave vector. Additionally, $E(\mathbf{r})$ and $H(\mathbf{r})$ describe the electric field for the TM modes and the magnetic field for the TE modes, respectively. The finite element method is employed to solve the equations, with the UC discretized into a 60×60 pixel grid. Each pixel is assigned a design variable x_e $(0 \leq x_e \leq 1)$ and the permittivity of each element, defined by its corresponding design variable, is interpolated via

$$\varepsilon(x_e) = \varepsilon_1(1 - x_e) + \varepsilon_2 x_e, \tag{2}$$

where ε_1 and ε_2 represent the permittivity of air ($\varepsilon_1 = 1$) and dielectric material, respectively. For on-chip applications, silicon with $\varepsilon_2 = 12$ is selected, though this can be adjusted to suit specific practical applications. Consequently, Eqs. (1) and (2) can be transformed into

$$\left(\mathbf{K} - \left(\frac{\omega}{c}\right)^2 \mathbf{M}\right) \mathbf{u} = \mathbf{0} \tag{3}$$

where $\mathbf{K}$ and $\mathbf{M}$ denote global matrixes (their detailed expressions can be referred to Ref. [47]) and $\mathbf{u}$ represents the eigenvector of the electric and magnetic fields for the TM and TE modes, respectively.

We set the optimization objective as maximizing the double odd-order bandgaps, formulated as [49]

$$\begin{aligned} \max : f &= \min(g_m, g_n) \\ &\approx -\frac{1}{\gamma}\ln\{\exp(-\gamma g_m) + \exp(-\gamma g_n)\} + \frac{1}{\gamma}\ln(2), \end{aligned} \tag{4}$$

where m and n represent the first and second odd-order bandgap orders, respectively. The aggregation parameter γ of the Kreisselmeier-Steinhauser function [49] is set at 20 in this case; g_o ($o = m$ or n) represents the relative bandgap size, which is expressed as

$$g_o = 2\frac{\min\ \omega_{o+1}(\mathbf{k}) - \max\ \omega_o(\mathbf{k})}{\min\ \omega_{o+1}(\mathbf{k}) + \max\ \omega_o(\mathbf{k})} \tag{5}$$

where $\omega_o(\mathbf{k})$ means the eigenfrequency for wave vector $\mathbf{k}$ of the oth band. To prevent numerical instabilities, the function g_o is further modified using the strategy outlined in Ref. [50] by overall considering ω_{o+1} and ω_o at all wave vectors.

Then, the gradient of the objective function about the design variable, x_e, can be obtained after calculating

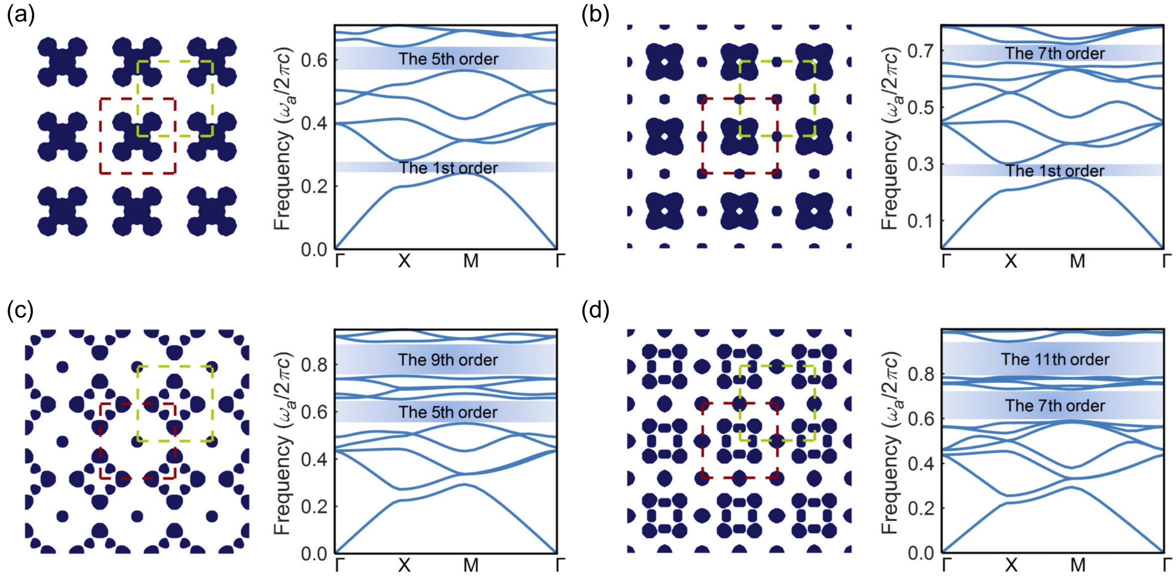

FIG. 1. Optimized PCs with different double odd-order bandgaps and the corresponding band diagrams for the TM modes. (a) PC with the first- and fifth-order bandgaps. (b) PC with the first- and seventh-order bandgaps. (c) PC with the fifth- and ninth-order bandgaps. (d) PC with the seventh- and eleventh-order bandgaps.

$\partial\omega_o(\mathbf{k})/\partial x_e$ and $\partial\omega_{o+1}(\mathbf{k})/\partial x_e$. Differentiating both sides of Eq. (3), $\partial\omega_o(\mathbf{k})/\partial x_e$ can be derived as $\partial\omega_o(\mathbf{k})/\partial x_e$, which is explicitly given by

$$\frac{\partial\omega_o(\mathbf{k})}{\partial x_e} = \frac{1}{2\omega_o}\mathbf{u}^{\mathrm{T}}\left(c^2\frac{\partial\mathbf{K}}{\partial x_e} - \omega_o^2(\mathbf{k})\frac{\partial\mathbf{M}}{\partial x_e}\right)\mathbf{u}. \tag{6}$$

After computing the derivative of the objective function about each design variable x_e, we employ the method of moving asymptotes (MMA) [51,52] to update the design variables iteratively until f is maximized. During the optimization, the UC is constrained with C_{4v} symmetry. We present the optimization procedures and the method to impose the constraint of C_{4v} symmetry in Secs. 2 and 3 within the Supplemental Material [46]. Note that, as initial designs play an important role in the topology optimization of photonic crystals, in some cases we first maximize one bandgap and then use the optimized structure as an initial

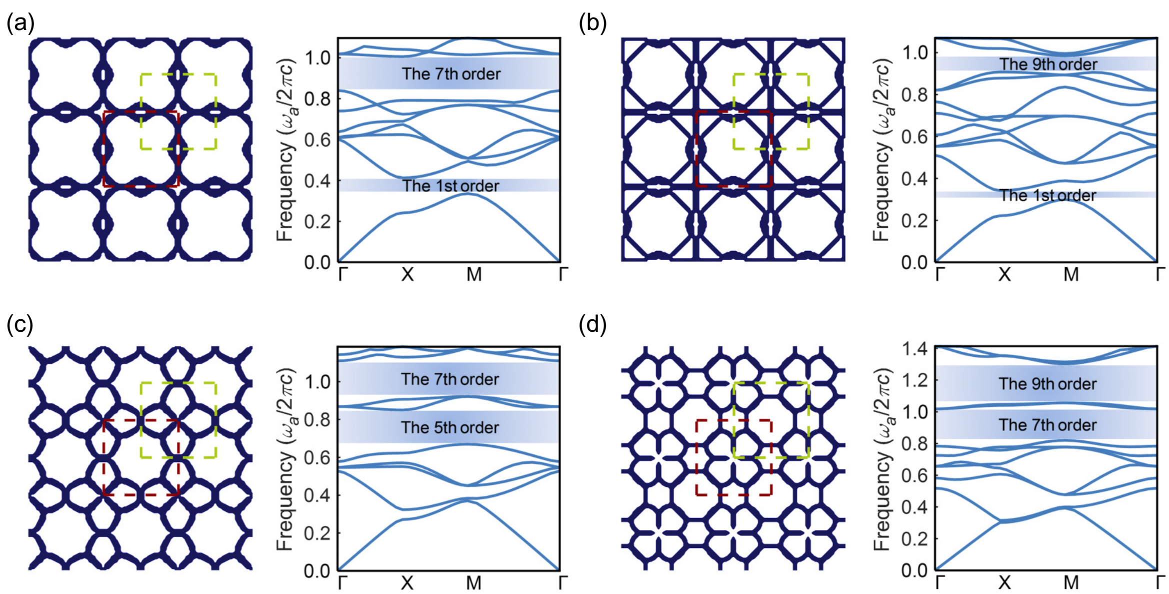

FIG. 2. Optimized PCs with different double odd-order bandgaps and the corresponding band diagrams for the TE modes. (a) PC with the first- and seventh-order bandgaps. (b) PC with the first- and ninth-order bandgaps. (c) PC with the fifth- and seventh-order order bandgaps. (d) PC with the seventh- and ninth-order bandgaps.

structure for the second-round optimization to obtain the final structure.

B. Customized PCs with dual topological bandgaps

To demonstrate the effectiveness of the developed design methodology for customizing PCs with on-demand dual odd-order bandgaps, we present several optimized PCs with various double odd-order bandgaps, denoted as different (m, n) pairs, for the TM and TE modes. Figures 1(a)–1(d) illustrate the optimized PCs along with the band diagrams for the TM modes with (m, n) set at (1, 5), (1, 7), (5, 9), and (7, 11), respectively. Similarly, Figs. 2(a)–2(d) show the optimized results for the TE modes with (m, n) set as (1, 7), (1, 9), (5, 7), and (7, 9), respectively. For simplicity, the frequency is expressed in a normalized form as $\Omega = \omega a/2\pi c$. The band diagrams reveal that the dual odd-order bandgaps with specified orders are successfully opened. The optimized PCs in Figs. 1(a)–1(d) are labeled as PCTM1, PCTM2, PCTM3, and PCTM4, respectively, while those in Figs 2(a)–2(d) are labeled as PCTE1, PCTE2, PCTE3, and PCTE4, respectively. The relative sizes of the first and second odd-order bandgaps are 14.5% and 12.5% for PCTM1, 17.7% and 9.5% for PCTM2, 16.9% and 17.2% for PCTM3, and 21.1% and 18.2% for PCTM4. For the TE modes, they are 20.5% and 18.0% for PCTE1, 13.3% and 8.2% for PCTE2, 23.8% and 18.5% for PCTE3, and 21.6% and 20.8% for PCTE4. Such wide dual bandgaps are conducive to producing highly localized dual-band corner states. Note that the developed method can also be used to design PCs with dual topological bandgaps of other desirable orders, and it can be further extended to design PCs with more topological bandgaps, as can be seen in the numerical examples in Sec. 5 within the Supplemental Material [46].

Two types of UCs are then picked from the same optimized PC in different ways: the first is the primitive UC (indicated by dark red lines in Figs. 1 and 2) and the other (indicated by cyan lines in Figs. 1 and 2) is the translation of the primitive UC by (a/2, a/2), where a is the lattice constant. We label the primitive UC selected from PCTMi and PCTEi in Figs. 1 and 2 as UCTMiA and UCTEiA, and the translated UC as UCTMiB and UCTEiB, respectively. Subsequently, we employ a 2D polarization [53–55] to characterize the topology property of these UCs, expressed by

$$P_j = \frac{1}{2}\left(\sum_l q_j^l \text{modulo } 2\right), (-1)^{q_j^l} = \frac{\eta_l(\mathrm{X}_j)}{\eta_l(\Gamma)} \tag{7}$$

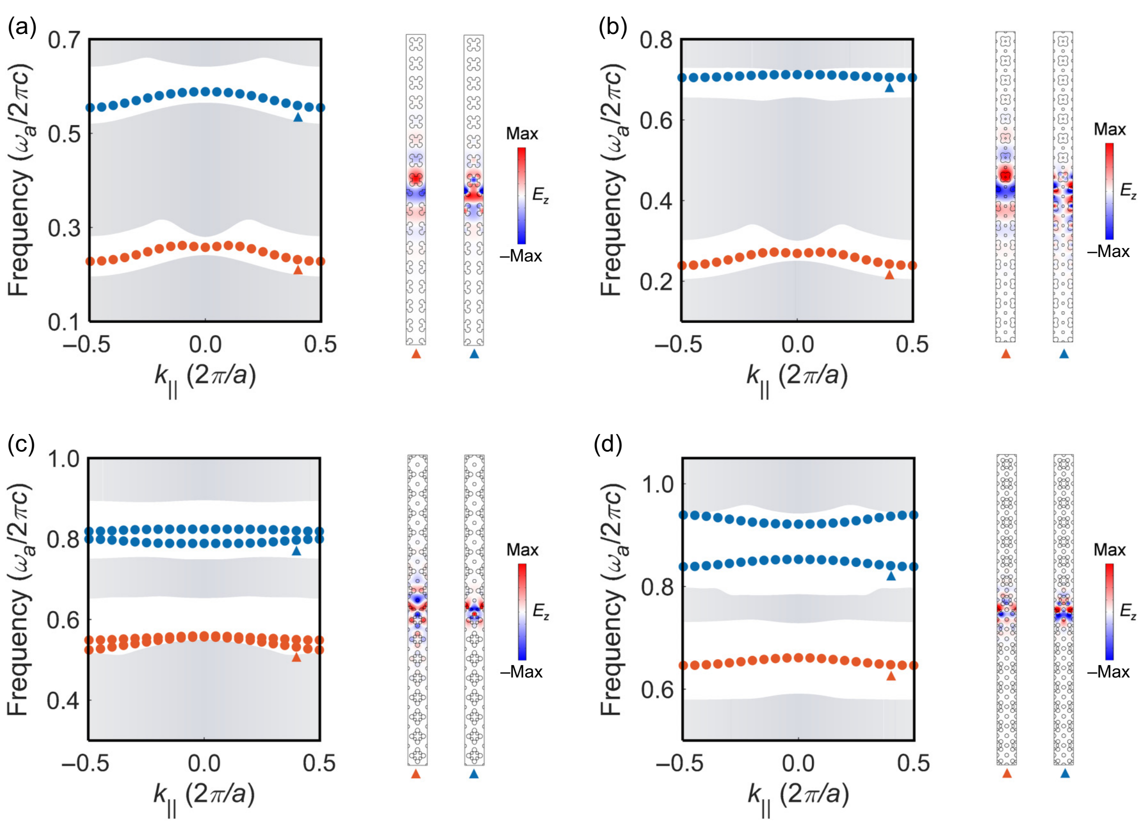

FIG. 3. Calculated projected band diagrams and eigenmodes of interface states for (a) SCTM1, (b) SCTM2, (c) SCTM3, and (d) SCTM4. The eigenmodes correspond to the solutions labeled by red and blue triangles in the band diagram.

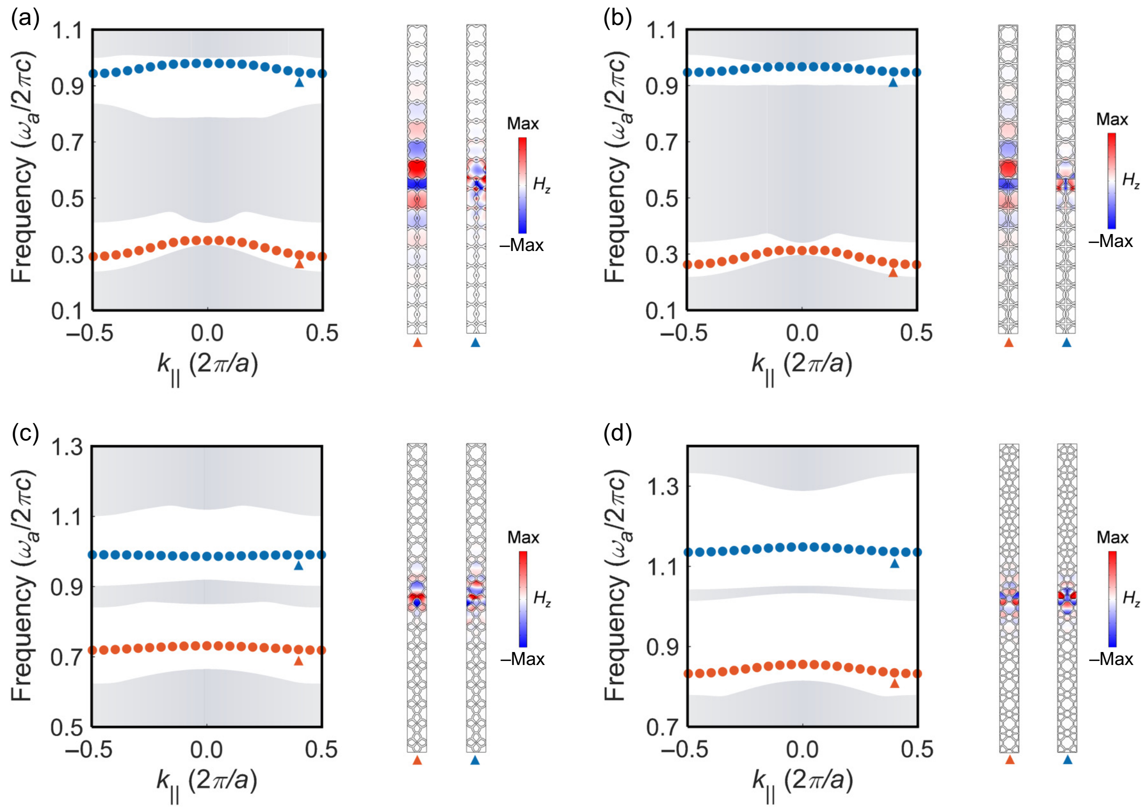

FIG. 4. Calculated projected band diagrams and eigenmodes of interface states for (a) SCTE1, (b) SCTE2, (c) SCTE3, and (d) SCTE4. The eigenmodes correspond to the solutions labeled by red and blue triangles in the band diagram.

where j represents the x- or y-direction and, as the optimized PCs are C_{4v} symmetric, $P_x = P_y$. Moreover, q_j^l can be determined according to the values of $\eta_l(\mathrm{X}_j)$ and $\eta_l(\Gamma)$, which are the parity ($\pm$) of the lth band at X and Γ, respectively. The parities of the eigenmodes are determined by their field profiles: monopolar and quadrupolar modes exhibit even parity ($+$), while dipolar modes have odd parity ($-$). The $\sum_l q_j^l$ means the sum of q over all the bands below the bandgap. Detailed parity information for UCTMiA, UCTMiB, UCTEiA, and UCTEiB is provided in Sec. 4 within the Supplemental Material [46]. By incorporating these parities into Eq. (7), we find that, for the TM modes, all UCTMiAs and UCTMiBs are trivial and nontrivial, respectively, for both the first and second odd-order bandgaps. For TE modes, UCTE1A and UCTE1B, UCTE2A and UCTE2B, UCTE3A and UCTE3B, and UCTE4B and UCTE4A are trivial and nontrivial, respectively, for the first odd-order bandgap, whereas UCTE1A and UCTE1B, UCTE2B and UCTE2A, UCTE3A and UCTE3B, and UCTE4A and UCTE4B are trivial and nontrivial, respectively, for the second odd-order bandgap. This indicates that, for both the first and second odd-order bandgaps, UCTMiA and UCTMiB (and UCTEiA and UCTEiB) consistently exhibit different topological properties. Consequently, dual-band topological interface states will emerge at the boundary between UCTMiA and UCTMiB (and UCTEiA and UCTEiB). Meanwhile, the simultaneous nonzero values of P_x and P_y lead to a topological corner charge [53–55], i.e.,

$$Q^c = 4P_xP_y. \tag{8}$$

Accordingly, we can derive that the corner charges for the aforementioned trivial and nontrivial UCs are 0 and 1, respectively. Therefore, it is predicted that the topological corner states can emerge at the corner shared by UCTMiA and UCTMiB (and UCTEiA and UCTEiB) within the two bandgaps.

C. Dual-band interface states

To confirm the existence of the predicted dual-band topological interface states at the boundary between trivial and nontrivial UCs, we build a supercell comprising eight trivial UCs and eight nontrivial UCs, with an interface between them, and calculate its projected band diagram. The supercell composed of UCTMiAs and UCTMiBs and UCTEiAs and UCTEiBs is labeled as SCTMi and SCTEi, respectively. Figures 3(a)–3(d) and 4(a)–4(d) present the calculated projected band diagrams and eigenmodes of the interface states of SCTM1–SCTM4 and SCTE1–SCTE4 for the TM and TE modes, respectively. The band diagrams reveal that topological interface states appear within

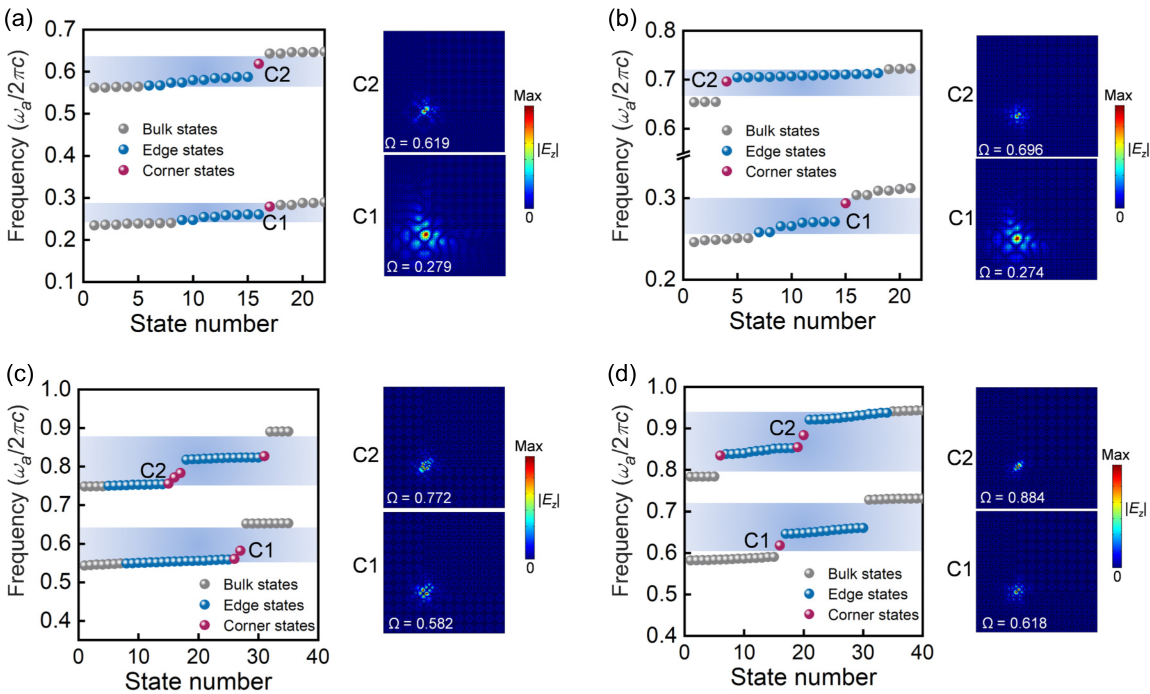

FIG. 5. Calculated eigenfrequency spectra and eigenfields of corner states for (a) MSTM1, (b) MSTM2, (c) MSTM3, and (d) MSTM4.

both the two designed bandgaps for all the supercells. The eigenfields of the interface states within these bandgaps, indicated by the red and blue triangles, demonstrate the localization of the energies at the boundary between trivial and nontrivial UCs. Crucially, these topological interface states are gapped, providing the necessary conditions for the formation of dual-band topological corner states.

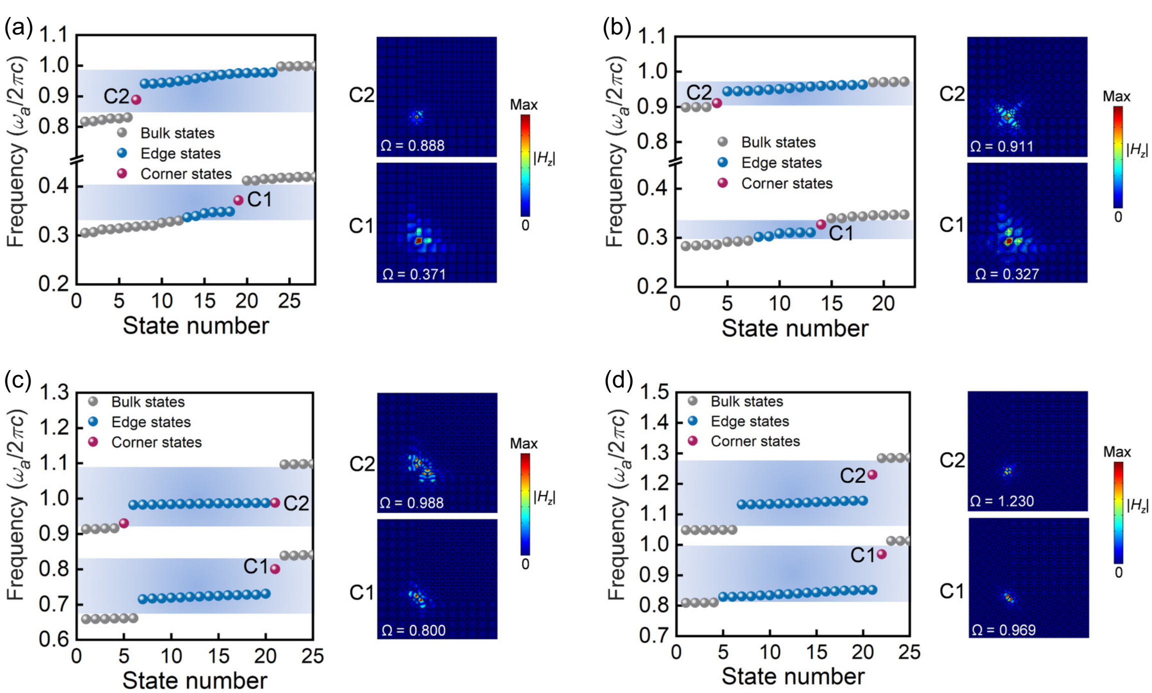

FIG. 6. Calculated eigenfrequency spectra and eigenfields of corner states for (a) MSTE1, (b) MSTE2, (c) MSTE3, and (d) MSTE4.

D. Dual-band corner states

To confirm the dual-band corner states, we construct a metastructure comprising an 8×8 array of UCTM*i*Bs or UCTE*i*Bs surrounded by four layers of UCTM*i*As or UCTE*i*As, forming a corner. This metastructure, composed of UCTM*i*As or UCTE*i*As and UCTM*i*Bs or UCTE*i*Bs, is labeled as MSTM*i* or MSTE*i*, respectively. Figures 5(a)–5(d) and 6(a)–6(d) present the calculated eigenfrequency spectra and eigenfields of the corner states for MSTM1–MSTM4 and MSTE1–MSTE4 in the TM and TE modes, respectively. The eigenfrequency spectra reveal that the corner states emerge within both bandgaps (highlighted in blue) across all the metastructures. The eigenmodes of the corner states, labeled C1 and C2, demonstrate the localization of the energies of these corner states at the corner. Additionally, multiple corner states within the same bandgap in MSTM3, MSTM4, and MSTE3 are observed, attributed to the long-range coupling effect induced by the irregular geometries identified through topology optimization. Notably, although we used a dielectric material with a permittivity of 12 during optimization, the corner states persist even when the dielectric material has a permittivity of 7.5, as detailed in Sec. 6 within the Supplemental Material [46].

E. Experimental validation of the dual-band corner states

Here, we use MSTM3 as an example to verify the dual-band corner states experimentally. To facilitate fabrication, we simplify the pillars shown in Fig. 1(c) into regular cylinders. According to the size of the pillars within the optimized structure, the simplified UCs, UCTM3A and UCTM3B [indicated by dark red and cyan boxes in Fig. 7(a), respectively], consist of two types of Al_2O_3

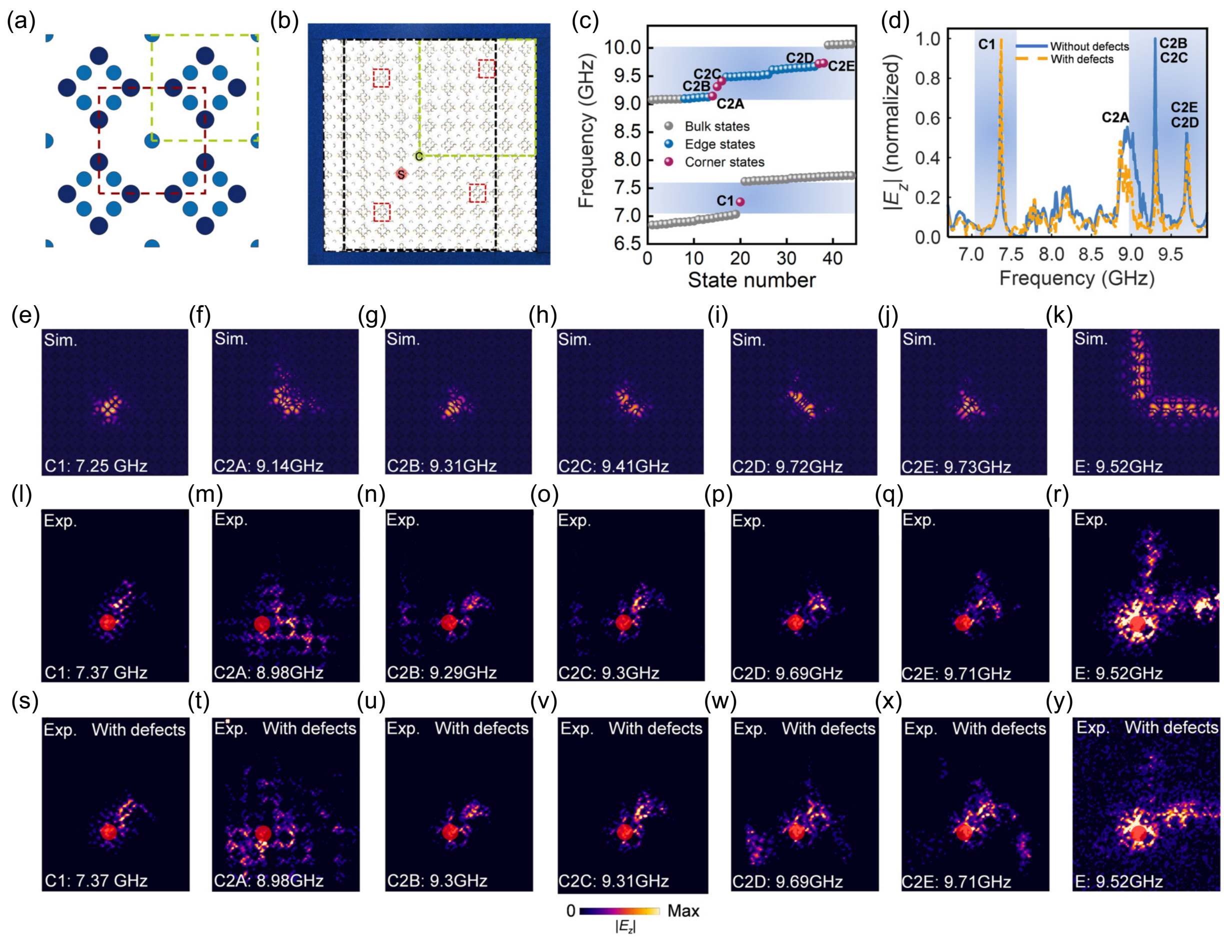

FIG. 7. Experimental validation of the dual-band corner states. (a) Sketch of the simplified UCTM3A and UCTM3B. (b) Fabricated sample. (c) Calculated eigenfrequency spectrum of the sample with an effective permittivity of 6.8. (d) Measured response of the electric field with respect to the frequency at the corner. (e)–(j) Numerically calculated eigenfields of corner states C1 and C2A–C2B. (k) Numerically calculated eigenfields of the interface state. (l)–(q) Experimentally measured electric fields of corner states C1 and C2A–C2B. (r) Experimentally measured electric fields of the interface state. (s)–(x) Experimentally measured electric fields of corner states C1 and C2A–C2B after introducing defects. (y) Experimentally measured electric fields of the interface states after introducing defects.

cylinders with diameters of 5 and 6 mm, represented by navy and blue circles, respectively, in Fig. 7(a). The permittivity of Al_2O_3 is 7.5 and the lattice constant is $a = 35.714$ mm (250/7 mm). To accommodate the experimental setup, the sample shown in Fig. 7(b) is made of a 6×6 array of simplified UCTM3Bs (denoted by the cyan box) surrounded by five layers of simplified UCTM3As, forming a corner labeled C. The sample is cladded by two parallel metal plates to create a quasi-2D condition. The Al_2O_3 cylinders are surrounded with microwave-absorbing materials to avoid unwanted scattering from the boundaries. In the microwave field mapping system, a monopole antenna as an excited source is introduced through a drilled hole in the bottom plate, while a probing antenna connected to a vector network analyzer (Keysight E5063A) measures the time-harmonic field distributions through the top plate. To ensure smooth movement during automatic measurements, a small air gap is maintained between the Al_2O_3 cylinders and the top plate, which may cause a frequency shift compared with the theoretical values. This can be corrected by reducing the permittivity of the dielectric materials in the numerical calculations [32]. Here, we use an effective permittivity of 6.8 to replace the genuine values to calculate the eigenfrequency spectrum of the sample, as presented in Fig. 7(c). One corner state (C1) appears within the first bandgap and five corner states (C2A–C2E) emerge within the second bandgap (the frequency windows of the first and second bandgaps are indicated by the blue areas). We positioned an excitation source close to the corner, as denoted by S in Fig. 7(b), and then captured the response of the electric field with respect to the frequency at the corner, as depicted in Fig. 7(d). A response peak is observed within the first bandgap, indicating the excitation of the corner state C1. Meanwhile, three response peaks are observed within the second bandgap. The first peak represents the excitation of corner state C2A. As the frequencies of corner states C2B and C2C (and C2D and C2E) are very close, the second and third peak indicates their excitation, respectively. Figures 7(e)–7(j) display the numerically calculated eigenfields of corner states C1 and C2A–C2E, while Figs. 7(l)–7(q) present the experimentally measured electric fields for these corner states [the scanning domain is indicated by the black dashed box in Fig. 7(b)], with the excitation points marked by the red circles. The measured electric fields accurately reflect the energy distributions of the numerically calculated eigenfields. Additionally, Figs. 7(k) and 7(r) show the calculated eigenfields and measured electric fields corresponding to the interface states at 9.52 GHz, demonstrating good agreement. Finally, we introduce defects by displacing the Al_2O_3 cylinders within the domains marked by the red boxes in Fig. 7(b) to validate the robustness of these corner states. The response spectrum captured at the corner, as shown in Fig. 7(d), continues to exhibit peaks corresponding to the frequencies of the corner states. The measured electric fields presented in Figs. 7(r)–7(s) further confirms that the corner and interface states remain excitable after introducing defects, validating their robustness.

III. CONCLUSIONS

In summary, we propose a way for customizing dual-band corner states in PCs. Several PCs with different dual-odd-order bandgaps of on-demand orders are designed via the topology optimization approach for both TM and TE polarizations. Based on these PCs, SPTIs with a highly localized interface and corner states within the customized double bandgaps are created. Furthermore, the multiple corner states, with their robustness, within dual bandgaps are experimentally validated. The developed design approach suggests a flexible way for engineering dual-band SPTIs to accommodate different application scenarios, which can also be extended to design multiband three-dimensional PTIs. Meanwhile, the designed dual-band SPTIs hold promise for advancing multiband topological photonic devices suitable for both linear and nonlinear optical applications.

ACKNOWLEDGMENTS

This work is supported by the National Natural Science Foundation of China (Grants No. 92263208 and No. 12102134), the Fundamental Research Funds for the Central Universities (Grant No. 2023ZDYQ11003), the State Key Laboratory of Millimeter Waves (Grant No. K202407), the Research Grants Council of Hong Kong SAR (Grants No. 15214323, No. 15200922, No. 15202820, and No. AoE/P-502/20), the Hong Kong Innovation and Technology Commission via project “Smart Railway Technology and Applications” (Grant No. K-BBY1), and the Faculty Development Scheme (FDS) RGC Project (Grant No. UGC/FDS24/E04/21).

DATA AVAILABILITY

The data that support the findings of this article are openly available [56].

[1] Z. Lan, M. L. Chen, F. Gao, S. Zhang, and E. Wei, A brief review of topological photonics in one, two, and three dimensions, Rev. Phys. **9**, 100076 (2022).

[2] L. Lu, J. D. Joannopoulos, and M. Soljačić, Topological photonics, Nat. Photonics **8**, 821 (2014).

[3] A. B. Khanikaev and G. Shvets, Two-dimensional topological photonics, Nat. Photonics **11**, 763 (2017).

[4] C. Feng, Y. Zhang, J. Shen, Z. Xu, Y. Dong, X. Fu, Y. Wang, L. Sun, X. Gan, and Y. Su, Ultra-low-power tunable topological photonic filter on hybrid integrated lithium tantalite and silicon platform, Laser Photonics Rev. **18**, 2300360 (2024).

[5] Y. Li, M. Jung, Y. Yu, Y. Han, B. Zhang, and G. Shvets, Topological directional coupler, Laser Photonics Rev. **18**, 2301313 (2024).
[6] F. Haldane and S. Raghu, Possible realization of directional optical waveguides in photonic crystals with broken time-reversal symmetry, Phys. Rev. Lett. **100**, 013904 (2008).
[7] S. Raghu and F. D. M. Haldane, Analogs of quantum-Hall-effect edge states in photonic crystals, Phys. Rev. A **78**, 033834 (2006).
[8] X.-T. He, E.-T. Liang, J.-J. Yuan, H.-Y. Qiu, X.-D. Chen, F.-L. Zhao, and J.-W. Dong, A silicon-on-insulator slab for topological valley transport, Nat. Commun. **10**, 872 (2019).
[9] X.-D. Chen, F.-L. Zhao, M. Chen, and J.-W. Dong, Valley-contrasting physics in all-dielectric photonic crystals: orbital angular momentum and topological propagation, Phys. Rev. B **96**, 020202 (2017).
[10] X. Ni, D. Purtseladze, D. A. Smirnova, A. Slobozhanyuk, A. Alù, and A. B. Khanikaev, Spin- and valley-polarized one-way Klein tunneling in photonic topological insulators, Sci. Adv. **4**, eaap8802 (2018).
[11] M. Saba, S. Wong, M. Elman, S. S. Oh, and O. Hess, Nature of topological protection in photonic spin and valley Hall insulators, Phys. Rev. B **101**, 054307 (2020).
[12] Y. Zeng, U. Chattopadhyay, B. Zhu, B. Qiang, J. Li, Y. Jin, L. Li, A. G. Davies, E. H. Linfield, B. Zhang, Y. Chong, and Q. J. Wang, Electrically pumped topological laser with valley edge modes, Nature **578**, 246 (2020).
[13] Z. Lan, J. W. You, Q. Ren, W. E. I. Sha, and N. C. Panoiu, Second-harmonic generation via double topological valley-Hall kink modes in all-dielectric photonic crystals, Phys. Rev. A **103**, L041502 (2021).
[14] X. Zhang, S. Li, Z. Lan, W. Gao, and M. L. Chen, Reconfigurable photonic valley filter in hybrid topological heterostructures, Laser Photonics Rev. **19**, 2400797 (2024).
[15] T. Long, X. Ma, J. Ren, F. Li, Q. Liao, S. Schumacher, G. Malpuech, D. Solnyshkov, and H. Fu, Helical polariton lasing from topological valleys in an organic crystalline microcavity, Adv. Sci. **9**, 2203588 (2022).
[16] L.-H. Wu and X. Hu, Scheme for achieving a topological photonic crystal by using dielectric material, Phys. Rev. Lett. **114**, 223901 (2015).
[17] D. Smirnova, S. Kruk, D. Leykam, E. Melik-Gaykazyan, D.-Y. Choi, and Y. Kivshar, Third-harmonic generation in photonic topological metasurfaces, Phys. Rev. Lett. **123**, 103901 (2019).
[18] L. J. Maczewsky, J. M. Zeuner, S. Nolte, and A. Szameit, Observation of photonic anomalous Floquet topological insulators, Nat. Commun. **8**, 1 (2017).
[19] M. C. Rechtsman, J. M. Zeuner, Y. Plotnik, Y. Lumer, D. Podolsky, F. Dreisow, S. Nolte, M. Segev, and A. Szameit, Photonic Floquet topological insulators, Nature **496**, 196 (2013).
[20] S. Mukherjee and M. C. Rechtsman, Observation of Floquet solitons in a topological bandgap, Science **368**, 856 (2020).
[21] B. Xie, H.-X. Wang, X. Zhang, P. Zhan, J.-H. Jiang, M.-H. Lu, and Y.-F. Chen, Higher-order band topology, Nat. Rev. Phys. **3**, 520 (2021).
[22] M. Kim, Z. Jacob, and J. Rho, Recent advances in 2D, 3D and higher-order topological photonics, Light: Sci. Appl. **9**, 130 (2020).
[23] H.-X. Wang, L. Liang, B. Jiang, J. Hu, X. Lu, and J.-H. Jiang, Higher-order topological phases in tunable C3 symmetric photonic crystals, Photonics Res. **9**, 1854 (2021).
[24] M. Li, D. Zhirihin, M. Gorlach, X. Ni, D. Filonov, A. Slobozhanyuk, A. Alù, and A. B. Khanikaev, Higher-order topological states in photonic kagome crystals with long-range interactions, Nat. Photonics **14**, 89 (2020).
[25] M. Li, Y. Liu, L. Tao, S. Ma, Y. Dong, Z. Li, L. Du, Y. Guo, K. Song, and X. Zhao, Evolution of an overlapped bandgap and topological flat bands in a higher-order valley photonic insulator based on dendritic structure, Laser Photonics Rev. **18**, 2300923 (2024).
[26] Q. Zhong, Y. Liang, S. Xia, S. Gao, L. Song, F. Hou, L. Tang, D. Song, and Z. Chen, Higher-order topological corner states in a specially distorted photonic kagome lattice, Laser Photonics Rev. **18**, 2301384 (2024).
[27] B. Xie, G. Su, H.-F. Wang, F. Liu, L. Hu, S.-Y. Yu, P. Zhan, M.-H. Lu, Z. Wang, and Y.-F. Chen, Higher-order quantum spin Hall effect in a photonic crystal, Nat. Commun. **11**, 3768 (2020).
[28] X.-D. Chen, W.-M. Deng, F.-L. Shi, F.-L. Zhao, M. Chen, and J.-W. Dong, Direct observation of corner states in second-order topological photonic crystal slabs, Phys. Rev. Lett. **122**, 233902 (2019).
[29] B.-Y. Xie, H.-F. Wang, H.-X. Wang, X.-Y. Zhu, J.-H. Jiang, M.-H. Lu, and Y.-F. Chen, Second-order photonic topological insulator with corner states, Phys. Rev. B **98**, 205147 (2018).
[30] B.-Y. Xie, G.-X. Su, H.-F. Wang, H. Su, X.-P. Shen, P. Zhan, M.-H. Lu, Z.-L. Wang, and Y.-F. Chen, Visualization of higher-order topological insulating phases in two-dimensional dielectric photonic crystals, Phys. Rev. Lett. **122**, 233903 (2019).
[31] L. Zhang, Y. Yang, Z.-K. Lin, P. Qin, Q. Chen, F. Gao, E. Li, J.-H. Jiang, B. Zhang, and H. Chen, Higher-order topological states in surface-wave photonic crystals, Adv. Sci. **7**, 1902724 (2020).
[32] X. Zhou, Z.-K. Lin, W. Lu, Y. Lai, B. Hou, and J.-H. Jiang, Twisted quadrupole topological photonic crystals, Laser Photonics Rev. **14**, 2000010 (2020).
[33] Y. Chen, Z. Lan, Z. Su, and J. Zhu, Inverse design of photonic and phononic topological insulators: a review, Nanophotonics **11**, 4347 (2022).
[34] Y. Chen, Z. Lan, and J. Zhu, Inversely designed second-order photonic topological insulator with multiband corner states, Phys. Rev. Appl. **17**, 054003 (2022).
[35] Y. Chen, Z. Lan, J. Li, and J. Zhu, Topologically protected second harmonic generation via doubly resonant high-order photonic modes, Phys. Rev. B **104**, 155421 (2021).
[36] Y. Chen, Z. Lan, and J. Zhu, Second-order topological phases in C4v-symmetric photonic crystals beyond the two-dimensional Su-Schrieffer–Heeger model, Nanophotonics **11**, 1345 (2022).
[37] S. Ma and S. M. Anlage, Microwave applications of photonic topological insulators, Appl. Phys. Lett. **116**, 250502 (2020).
[38] W. Zhang, X. Xie, H. Hao, J. Dang, S. Xiao, S. Shi, H. Ni, Z. Niu, C. Wang, K. Jin, X. Zhang, and X. Xu, Low-threshold topological nanolasers based on the second-order corner state, Light: Sci. Appl. **9**, 109 (2020).

[39] Y. Ota, F. Liu, R. Katsumi, K. Watanabe, K. Wakabayashi, Y. Arakawa, and S. Iwamoto, Photonic crystal nanocavity based on a topological corner state, Optica **6**, 786 (2019).

[40] X.-T. He, M.-Y. Li, H.-Y. Qiu, W.-S. Ruan, L.-D. Zhou, L. Liu, X.-D. Chen, W.-J. Chen, F.-L. Zhao, and J.-W. Dong, In-plane excitation of a topological nanophotonic corner state at telecom wavelengths in a cross-coupled cavity, Photonics Res. **9**, 1423 (2021).

[41] S. S. Kruk, W. Gao, D.-Y. Choi, T. Zentgraf, S. Zhang, and Y. Kivshar, Nonlinear imaging of nanoscale topological corner states, Nano Lett. **21**, 4592 (2021).

[42] K. H. Kim and K. K. Om, Multiband photonic topological valley-Hall edge modes and second-order corner states in square lattices, Adv. Opt. Mater. **9**, 2001865 (2021).

[43] Z. Liu, D. Zhu, L. Raju, and W. Cai, Tackling photonic inverse design with machine learning, Adv. Sci. **8**, 2002923 (2021).

[44] B. MacLellan, P. Roztocki, J. Belleville, L. Romero Cortés, K. Ruscitti, B. Fischer, J. Azaña, and R. Morandotti, Inverse design of photonic systems, Laser Photonics Rev. **18**, 2300500 (2024).

[45] M. Park, L. Grbčić, P. Motameni, S. Song, A. Singh, D. Malagrino, M. Elzouka, P. H. Vahabi, A. Todeschini, W. A. de Jong, R. Prasher, V. Zorba, and S. D. Lubner, Inverse design of photonic surfaces via high throughput femtosecond laser processing and tandem neural networks, Adv. Sci. **11**, 2401951 (2024).

[46] See Supplemental Material at http://link.aps.org/supplemental/10.1103/PhysRevApplied.23.044048 for the parity variation of eigenmodes at the Γ and X points by shifting the lattice, the procedure of the topology optimization method, the method to impose the constraint of C_{4v} symmetry, the parities at high-symmetry points of unit cells, the additional optimized dual-band and triple-band PTCMs, and eigenfrequency spectrum of the metastructure when the permittivity of the dielectric materials is 7.5.

[47] Y. Chen, F. Meng, J. Zhu, and X. Huang, Inverse design of second-order photonic topological insulators in C3-symmetric lattices, Appl. Math. Model. **102**, 194 (2022).

[48] J. D. Joannopoulos, S. G. Johnson, J. N. Winn, and R. D. Meade, *Photonic Crystals: Molding the Flow of Light* (Princeton University Press, New Jersey, 2011).

[49] Y. Li, Y. Luo, and X. Zhang, Topological design of phononic crystals for multiple wide band gaps, J. Sound Vib. **529**, 116962 (2022).

[50] F. Meng, X. Huang, and B. Jia, Bi-directional evolutionary optimization for photonic band gap structures, J. Comput. Phys. **302**, 393 (2015).

[51] J. Nocedal and S. J. Wright, *Numerical Optimization* (Springer, New York, 1999).

[52] K. Svanberg, A class of globally convergent optimization methods based on conservative convex separable approximations, Soc. Ind. Appl. Math. **12**, 555 (2002).

[53] F. Liu, H.-Y. Deng, and K. Wakabayashi, Helical topological edge states in a quadrupole phase, Phys. Rev. Lett. **122**, 086804 (2019).

[54] Z. Zhang, M. R. López, Y. Cheng, X. Liu, and J. Christensen, Non-Hermitian sonic second-order topological insulator, Phys. Rev. Lett. **122**, 195501 (2019).

[55] Z. Zhang, H. Long, C. Liu, C. Shao, Y. Cheng, X. Liu, and J. Christensen, Deep-subwavelength holey acoustic second-order topological insulators, Adv. Mater. **31**, 1904682 (2019).

[56] Yafeng, Chen, Original experimental data of “Topology optimization empowered dual-band second-order photonic topological insulators”, Harvard Dataverse, draft version, 2025, https://doi.org/10.7910/DVN/KGN2TE.